

Rainfall Estimation method using Satellite imagery over South America

Germán Delgado¹, Luiz Augusto Toledo Machado², Carlos Frederico Angelis², Marcus Jorge Bottino², Ángel Redaño¹, Jerónimo Lorente¹, Luis Gimeno³, Raquel Nieto³

¹ Astronomy and Meteorology Department, University of Barcelona, Barcelona (Spain)

² Instituto Nacional de Pesquisas Espaciais, Centro de Previsto de Tempo e Estudos Climaticos, Cachoeira Paulista-SP (Brazil)

³ Universidad de Vigo, Facultad de ciencias de Ourense, Ourense, Spain

Abstract

The importance of the relationship between the life cycle of the mesoscale convective system (MCS) and the rainfall rate it produces has been reported in several works. In spite of that, a specific quantification of this relationship has not been found. Our aim was to find an empirical relationship between the characteristics that describe the MCS life cycle and the amount of rainfall rate it produces in order to develop a rainfall rate estimation algorithm. This paper reports a rainfall satellite estimation technique using the Precipitation Radar product (PR) onboard the TRMM Satellite, GOES IR (10.5 μm) brightness temperature (T_b), an IR-VIS (0.65 μm) cloud classification and radiative properties of clouds over the life cycle of deep convective systems. Numerous earlier studies focus on this subject using patch or pixel-based techniques. We use both techniques with satisfactory results when compared with the Hydroestimator technique. The algorithm first associates rain with the colder pixels belonging to a certain cloud type (convective clouds, cumulus and cold stratiform clouds). The rainfall estimation is carried out using the MCS properties (expansion and difference mean temperature among others), the internal brightness temperature (T_b) variability of the pixel for every cloud type and some statistical assumptions. The method performs reasonably well in the case of convective, but also for stratiform rainfall, although it tends to overestimate rainfall rates values.

1. Introduction

Several works focus on the rainfall rate estimation using IR VIS imagery highlighting its importance due to the low sampling of the ground-based radars and the sparse distribution of the rain gauges. Satellite estimations provide high spatial and temporal sampling frequencies, but the information is inferred through indirect methods leading to significant errors in both rain / no rain discrimination and rainfall rate estimation. Previous works report the applications of satellite rainfall rate estimation in hydrological, meteorological and climatological sciences: flood forecasting, validation rainfall forecast from numerical weather prediction (NWP) models, moisture budget studies and evaluation of climate models (Adler and Negri, 1988; Ba and Gruber, 2001; Kuligowski, 2002; Xu et al., 1999; Vicente et al., 1998; Ebert et al., 1996). Laing et al. 1999 emphasise the influence of rainfall on agriculture and how monitoring it can help to reduce human injuries during floods. For these reasons Kidd et al., 2003, draws attention to the importance of suitable satellite rainfall rate estimation monitoring in the economy.

The IR satellite rainfall estimate has been a topic of study since the late 1970s. The hydroestimator technique (Vicente et al., 1998; Vicente et al., 2002) is based on the methodology developed by Scofield (1987) and uses a non-linear power law relationship between the top cloud temperature and the radar-derived rainfall rate estimates, a gradient and growth rate mask and a humidity mask to compute rainfall rates. The hydroestimator technique (HE) was developed to estimate intense convective systems rainfall rates. Arkin and Meisner (1987) developed the GOES precipitation index (GPI) method, which explores statistical relationships between cloud top temperatures and rainfall. The technique assigns a mean rainfall rate to all the pixels below a threshold temperature. The GPI is more indicated to estimate monthly

cumulated rainfall than shorter time range estimates. The GOES Multispectral Rainfall Algorithm (GMSRA) is described by Ba and Gruber (2001). The method uses five channels from the GOES satellite and incorporates cloud-top particle information by taking advantage of the spectral resolution. As well as the HE, GMSRA uses an additional moisture correction factor to account for evaporation of rainfall falling from the clouds and not reaching the surface (Kidd et al., 2003). Both HE and GMSRA estimates improve the GPI, with better correlations, BIAS and RMS. Laing et al. (1999) present a relationship between SSM/I-derived precipitation characteristics and IR data to estimate the precipitation produced by African mesoscale convective complexes (MCC). The precipitation is diagnosed using the IR-observed cold cloud area as a function of time of the MCC's life cycle. Xu et al. (1999) presents a method for identification and removal of no-rain cold clouds from IR imagery. Seven cloud patch features are used to describe cloud-top properties and produce classification rules. Lastly, Hsu and Gao (2004) describe the Precipitation Estimation from Remotely Sensed Information using Artificial Neural Networks (PERSIAN) Cloud Classification System (CCS). Local and regional cloud features are extracted to calibrate the cloud-top temperature and rainfall relationships for the classified cloud groups. The results show good correlations coefficients at 0.25 degree grid size boxes.

This work presents a new Rainfall Estimation method using Satellite imagery (RESAT) for the area of South America. This region, which includes the Amazonian forest, covers a tropical and sub-tropical area where the formation of MCS with the potential to produce heavy rainfall is common. This makes RESAT a valuable tool in order to monitor not only convective but also stratiform rainfall in the zone.

All the works mentioned above can be classified as pixel-based or cloud patch-based methods and all of them have a bearing on this paper. The RESAT algorithm is based

on both pixel and cloud patch properties. Feidas and Cartalis (2001), Manthon et al. (2002) and Schumacher and Johnson (2005) point out the importance of the relationship between the life cycle of MCS and the rainfall rate it produces. In this work a cluster rainfall estimation is first computed using some radiative and evolution parameters over the MCS life cycle and then a pixel estimation is obtained by adding a correction using cloud-top pixel radiative properties. Uddstrom and Gray (1996) obtain 60 % upward accuracy in delineate raining and non-raining samples of a cloud classification showing the sensibility of the final rainfall estimation on the cloud type. That's why an IR-VIS cloud classification is also used in order to assign different coefficients to each cloud type in the final rainfall rate estimation and also to decide the rain / no rain discrimination.

2. Data and satellite products

All the data used in this work is provided by the satellite division (DSA) of the Centro de Previsão do Tempo e Estudos Climáticos (CPTEC), which belongs to the Instituto Nacional de Pesquisas Espaciais (INPE) located in the State of São Paulo, Brazil (Carlos Federico Angelis et al., 2005). The satellite division receives data from many satellites such as GOES, METEOSAT, TERRA, ACQUA and NOAA. The satellite products used in this work are produced in the DSA in real time: an IR-VIS cloud classification, an improved version of the NESDIS Hydroestimator (Vicente et al., 1998) and an operational product called ForTraCC (Forecast and Tracking of Active Convective Cells) that tracks mesoscale convective systems (MCS) and displays information on the expansion, speed and other parameters of the systems (Machado et al., 1998; Machado et al., 2003; Vila et al., 2005).

Two months of Tropical Rainfall Measuring Mission (TRMM) and precipitation radar (PR) data over South America during November and December of 2004 were also provided by the CPTEC's satellite division. The PR scans a 215 km swath with an 80 vertical range bins extending to 20 km above the earth ellipsoid. The vertical and horizontal resolutions are 250 m and $4.3 \times 4.3 \text{ km}^2$ respectively, at nadir, while the minimum detectable signal is approximately 17 dBZ.

The cloud classification is carried out using a cluster analysis with IR and VIS GOES images, thus the classification is only operative during the daytime. The basis of the algorithm has been described in several works (Porcú and Levizzani, 1992; Rossow and Palmer, 1993; Delgado et al., 2005), therefore only a brief description is provided here. Four parameters are used to create a multispectral histogram: the IR brightness temperature (T_b), the visible reflectivity and two texture indexes computed as the Standard Deviation between the first neighbours of each pixel in both channels. Each point in the histogram corresponds to the number of pixels in the image with the same four parameters values. After an analysis of the cluster distribution in the multispectral histogram over several months, 30 seed points are chosen. Every seed point has four components corresponding to each of the four parameters described below and will flag a class in the histogram. In order to have a proper calibration of the classification algorithm, that is to say, a physical correspondence between the values of the parameters defining each seed point and a cloud or surface type, these parameters will acquire a different value depending on the time of the day. Three daily segments are used: morning, midday and afternoon. The algorithm associates each point in the multispectral histogram with the closest seed point, minimizing the Euclidean Distance. The main classes obtained are Surface (3 types), Cumulus (10 types), Cirrus (6 types), Stratus (5 types) and Multilayer (6 types).

The high temporal resolution of GOES allows the development of operational methods to obtain information on the monitoring of meteorological phenomena such as the expansion and shifting velocity of MCS. The expansion, mean temperature difference and other parameters of MCS used in this paper and defined below are obtained using the ForTracC. The technique is based on an algorithm that allows tracking of the MCS, computing the radiative and morphological properties and forecasting the evolution of these physical properties (based on cloud-top brightness temperature) up to 120 minutes, using infrared satellite imagery. The algorithm consists of four steps (Vila et al., 2005):

1. A cloud cluster detection method based on a size and temperature threshold
2. A statistical module to perform morphological and radiative parameters of each MCS.
3. A tracking technique based on MCS overlapping areas between two successive images.
4. A forecast module based on MCS evolution in previous time steps.

The 4th step is not used in this work. The algorithm is based on the work of Machado et al. (1998). The author analyzes the life cycle of convective systems and suggests that the surface expansion of a convective system could be associated with the high-level of wind divergence and the length of its life cycle.

The results of the rainfall rate estimation algorithm presented in this work is compared with the estimations of the improved version of the NESDIS Hydroestimator (Vicente et al., 1998), hereafter known as DSA Hydroestimator, which assimilates GOES (10.5 μm) and METEOSAT (11.5 μm) data, wind and humidity data produced by the CPTEC's numerical weather forecast model (ETA model) and topography information. The NESDIS Hydroestimator mathematical function, which assesses rainfall for each GOES

pixel, is shifted upwards or downwards according to a combination of factors derived from all information assimilated by the DSA Hydroestimator. These improvements on the NESDIS Hydroestimator were made in order to estimate rainfall over the South America more accurately, mainly in its tropical part.

We also extract the cloud top temperature from the IR GOES channel. All the data used in this work (including the IR GOES images, the PR TRMM product, the IR-VIS cloud classification, the DSA Hydroestimator maps and the arrays containing the values of the parameters of each MCS considered) have been reprojected to a mercator projection with a spatial resolution of 0.038° of longitude and 0.036° of latitude.

Several restrictions were applied in order to select the cases of study within 2 months of data. Due to the use of the Visible GOES channel to obtain the cloud classification only daily data were chosen. There is a ± 15 min time difference and a maximum navigation error of 10 km between the TRMM pass and the IR GOES scanning. The IR data closest to the time of the TRMM observation were chosen to obtain a final time difference of less than ± 5 min and a navigation error of less than 1 pixel. Finally the availability of GOES images covering the Southern Hemisphere is not assured by NOAA for many reasons, so when images are missed, no products are generated. This was a final restriction we found in order to select the cases. In total 27 cases were selected for the study; 18 during the analysed period and 9 for validation tasks. Table 1 summarises the date and hour of all the selected cases.

The South America region is the domain chosen for this study (figure 1). All the cases are located inside of the following window centred over Brazil: 35 S, 5 N, 35 W, 75 W.

3. Description of the algorithm

All the published works concerning rainfall rate estimation mentioned in the introduction develop the estimation technique through general assumptions. In our case we assume similar facts, taking into account the importance of the development stage of the convective system and the cloud classification. Scofield (1987) summarises some of these assumptions as having an especial importance the fact that

1. clouds with cold tops in the IR imagery and high reflectivity in the VIS imagery produce more rainfall than those with warmer tops and
2. low reflectivity and decaying clouds produce little or no rainfall, whereas clouds in forming stage tend to produce heavy rainfall.

We don't work directly with the Visible channel, although the information of this channel is contained in the cloud classification, thus those clouds with a high reflectivity top (convective in the cloud classification) will have different treatment in the algorithm. In fact every cloud type will have different parameterization in the algorithm. We also pay attention to the MCS's internal brightness temperature variability, and not only in the value of T_b . Concerning the second general approach mentioned above, different parameters of the evolution of each convective system will be computed using the ForTracC. These parameters (like the expansion or the mean temperature difference between one system in two consecutive images) will describe the stage of each convective system along its life cycle and its dynamic conditions. As we explain in section 3.3 those convective systems in a growing phase (some of them in an exploding phase during its initial stage) will have associated a high value of rainfall rate.

Other works (Wylie, 1979; Hsu and Gao, 2004) focus on the importance of working with different T_b thresholds in order to detect correctly the convective cells embedded in

the MCS. Convective cells are the colder pixels in a convective system, although they are smaller they produce heavier rainfall. As we explain in next section, five different T_b thresholds are considered in this work in order to associate the proper dynamic parameters to the convective cells embedded in the detected convective systems. This hypothesis helps to decrease the errors in the final rainfall rate estimation.

Many authors (Mapes and Houze, 1993; Machado and Rossow, 1993; Machado et al., 1998) consider that $T_b \leq 245$ K is a satisfactory threshold to identify MCS. The near-linear dependence between the convective system area and its threshold indicates the insensitivity of the choice of a specific value in a range of 10-20 K (Carvalho and Jones, 2001). In order to have a wider range of brightness temperature in the algorithm estimations, pixels colder than 250 K are considered to form part of a MCS.

3.1. Threshold divisions

The RESAT is based on the correlation between the radiative and evolution parameters of the convective systems and its mean rainfall rate. Therefore only pixels colder than 250 K are considered for the estimation. A deep convective cloud system is identified by adjacent satellite image pixels with an infrared brightness temperature colder than a given threshold. In order to separate effectively the convective cells contained in the MCS the following structure and evolution parameters are computed for the IR cloud clusters with T_b colder than five different thresholds (250 K, 240 K, 230 K, 220 K and 210 K): Mean and Minimum Temperature (T_m and T_{min}), Mean Temperature difference between two consecutive images (ΔT_m), Minimum temperature difference between two consecutive images (ΔT_{min}) and the expansion computed as the normalized difference between areas divided by time (30 min) in two consecutive images, defined as $\Delta E = 1/A * (dA/dt)$ (see Machado et al., 1998, Machado and Laurent, 2004, Vila et al., 2005), where A is the area of a given MCS in a given time. Each T_b threshold will define a

concentric layer (see figure 2), being the most external the one defined as all the pixels colder than 250 K (layer 1) and being the most internal the one defined as all the pixels colder than 210 K (layer 5). Both rain / no rain discrimination and rainfall rate estimation will be computed for each of the cloud layer obtained by applying the multilayer tracking algorithm, and summarised in the flow chart of figure 2.

The algorithm will first assign the value of the estimated rainfall computed for the first layer of each MCS. If the MCS has been divided in more layers, the algorithm will superpose the estimated values of rainfall rate to the pixels in the second layer. The process will continue for the rest of the layers until the last one.

The difference between T_b of each pixel and T_m of the cloud cluster where the pixel is located is also used. Henceforth this T_v variable gives us an idea of the T_b internal variability of the MCS. Pixels with negatives values of T_v will be located in the coldest region of the layer with a higher probability of having rainfall associated. As previously mentioned, one of the assumptions in satellite rainfall estimation works is that colder pixels have been associated with more rainfall than warmer ones. The definition of T_v helps us to discriminate better between two pixels with the same T_b but different value of the rainfall rate associated.

3.2. Rain / no Rain discrimination

Nearly 97% of the rain pixels of the selected cases during the analysed period are classified in six cloud types: 4 types as convective clouds, one as cold stratiform cloud and one as cumulus (a single cumuliform vertically developed cloud in its first stage of development). One of the four convective types is flagged as a Deep Convective Cloud (DCC) and the other convective ones can be interpreted as the coldest part of the anvil of the DCC in different temperature ranges. We will refer to these three as convective (C1, C2 and C3) to differentiate them from DCC. Pixels classified as C1 are the colder

ones, being located close to the cold core (DCC) of the MCS, their reflectivity in the VIS channel is also higher. Pixels classified as C2 are also colder than C3, but with similar values of VIS reflectivity and considerable differences in the texture indexes, being C3 the roughest and C2 the smoothest.

The percentage of pixels of each class in each layer of each MCS is computed. Each layer is associated with the class containing more pixels. Only MCS layers associated with the raining cloud types mentioned above are classified as rain clusters. Only pixels belonging to the six cloud types mentioned above in each layer classified as a rainy is flagged as a possible rain pixel. The final rain / no rain discrimination depend on the cloud type:

- a. Cumulus pixels embedded in layers associated with convective, DCC and cold stratiform cloud types are classified as rain pixels. Those embedded in layers associated with cirrus are not classified as rain pixels.
- b. Cold stratiform pixels embedded in layers associated with DCC and cold or warm stratiform cloud types are classified as rain pixels.
- c. Convective pixels embedded in layers associated with convective, DCC and cold stratiform cloud types and with $T_v < 0$ are classified as rain pixels.
- d. DCC pixels embedded in layers associated with DCC and convective cloud types and with $T_v < 0$ are classified as rain pixels.

3.3. Rainfall rate estimation

The rainfall rate estimation of the pixels classified as rain pixels consists of three steps. In the first step the mean rainfall rates from the radar data are computed for each MCS for each T_b Threshold. This value is compared with the parameters describing the evolution stage of the MCS for the same T_b threshold. A multiple linear regression is computed between these variables and the mean rainfall rate. A value of rain (the cluster

rainfall estimation, R_c) is associated with each layer of each MCS by superposing the value of R_c for each T_b threshold.

In the second step of the rainfall rate estimation, T_v is used in order to assign a more accurate value of rainfall rate to each pixel, the pixel rainfall estimation (R_p). In this step a pixel correction (pixel rainfall correction, r_c) is added to R_c using a non-linear relation between T_v and the radar data for each pixel of the MCS in a given layer.

In the third step, the frequency distribution computed over all the cases of the analysed period of the radar data and R_p will be approximated to an exponential distribution. R_p cumulated distribution will be fitted to the radar data one in order to increment its range and obtain the final value of the estimated rainfall rate R .

3.3.1. Cluster rainfall estimation

A multiple linear regression is computed between ΔE , T_m , ΔT_m , T_{min} , ΔT_{min} and the mean radar rainfall rate for each T_b threshold in each MCS. Thus, each pixel from the same MCS and in the same layer is associated with the same rainfall cluster term (R_c) given by the following expression:

$$R_c = a_i * \Delta E + b_i * T_m + c_i * \Delta T_m + d_i * T_{min} + e_i * \Delta T_{min} + f_i \quad (1)$$

where i is the layer, a_i , b_i , c_i , d_i and e_i are the linear coefficients for each variable and f_i is the constant term. Figure 3 shows the mean radar rainfall rate versus the different cluster parameters for a 230 K threshold. Similar plots are obtained for the rest of the T_b threshold. Table 2 shows the coefficients and its correlation index of the multiple linear regression for each T_b threshold. Using (1), a value of R_c is assigned to all the pixels of one MCS in each layer. First, all the pixels of the MCS are assigned with the value of R_c computed for the first T_b threshold (pixels colder than 250 K), then the value of R_c

computed for the second T_b threshold (pixels colder than 240 K) is superimposed to the first one, the same occurs with the other values of R_c for the rest of the T_b threshold. When the process ends each layer in the MCS has associated a value of R_c . Figure 4 shows the mean radar rainfall rate versus R_c computed for all the T_b threshold.

3.3.2. Pixel rainfall estimation

In the second step the following rainfall rate will be assigned to each pixel belonging to one of the 6 cloud types able to produce rainfall:

$$R_p = R_c + r_c \quad (2)$$

where r_c is the result of the comparison between the mean value of the difference between the radar value and R_c for each 1 K interval of T_v , therefore R_p is a function of T_v and the cloud type. A similar methodology is used in Vicente et al. (1998). Figure 5 shows this relationship for the 6 cloud types considered. The points were fitted to a three degree polynomial curve. Table 3 summarises the coefficients of the polynomial curve for all the cloud types.

Both R_c and r_c contribute to the value of R_p . R_c is the cluster contribution and its value depends on the radiative and evolution parameters that characterise each MCS, whereas r_c is the pixel contribution to the total rainfall rate and is a function of T_v , which gives an idea of the value of the spatial temperature gradient within the MCS. However, both contributions are derived as functions of the mean value of the radar data. As a consequence, the range of R_p in the cumulated frequency distribution is smaller than the range of the radar data (figure 6), but both radar and R_p distributions fit into an exponential distribution. In order to validate this assumption, the average value of the radar data in different grid sizes was also computed and its spatial distribution was

compared to the R_p distribution. The greater the grid size, the more similar the ranges of both distributions.

3.3.3. Range increment

In the third step of the rainfall rate estimation both radar and R_p frequency distributions will be approximated to an exponential probability density function (pdf) for each cloud type. The final value of the estimated rainfall rate R will be given by fitting the R_p exponential pdf to the radar exponential pdf. Figure 6 shows both distributions in the case of DCC. To fit one pdf into the other we assume the following approximation: the radar data pdf and the final estimated rainfall rate pdf will have the same decayment. The fitting method associates a certain value of R_p with the value of the radar data having the same decayments in both exponential pdfs. This value associated to R_p will be the final rainfall rate estimated value, R . An exponential probability density function is defined by:

$$f(t) = \lambda * \exp(-\lambda * t) \quad (3)$$

where λ is the rate parameter of the distribution, $1/\lambda$ is the mean value of the distribution and $1/\lambda^2$ is the variance of the distribution. The R_p and radar distribution will have the following exponential pdf associated:

$$f_{R_p} = \lambda_{R_p} * \exp(-\lambda_{R_p} * R_p) \quad (4)$$

$$f_r = \lambda_r * \exp(-\lambda_r * r) \quad (5)$$

We associate the values of r and R_p with the same decayment through the following expression:

$$f_{R_p} / \lambda_{R_p} = f_r / \lambda_r, \quad (6)$$

which leads to

$$\exp(-\lambda_{R_p} * R_p) = \exp(-\lambda_r * r) \quad (7)$$

by isolating the r we obtain

$$r = (\lambda_{Rp} / \lambda_r) * R_p \quad (8)$$

Finally we apply the above approximation to obtain the final rainfall estimation, R , as a function of R_p , λ_{Rp} and λ_r

$$R(R_p, \lambda_{Rp}, \lambda_r) = (\lambda_{Rp} / \lambda_r) * R_p. \quad (9)$$

Table 4 summarises the values of λ_{Rp} and λ_r for all the accumulated histograms of the different cloud type.

4. Results

Several statistical measures are used to compare the rainfall rate estimation with the radar data. In the case of the rain / no rain discrimination we use the False Alarm Ratio (FAR), the Probability of Detection (POD), the Error (ERR) and the Frequency Bias Index (FBI). The range of POD, FAR and ERR is 0 to 1. FAR and ERR perfect score is 0 and POD perfect score is 1. Values of FBI greater than 1 indicate overestimation and less than 1 indicate underestimation.

In the case of the rainfall estimation the correlation coefficient, the RMSE, the BIAS and the standard deviation are used. Values of BIAS greater than 0 indicate overestimation and negative values underestimation.

RESAT is compared with the Hydroestimator method (Vicente et al., 1998). HE uses a non-linear power law relationship between the top cloud temperature and radar-derived rainfall estimates to compute rainfall rates. HE uses a gradient and a growth rate mask to make the rain / no rain discrimination. The main differences between both methods are that the HE doesn't take into account the cloud types and uses a humidity mask instead of the properties of convective systems. The HE was originally developed to estimate intense convective systems rainfall rates.

4.1. Rain /no Rain

Table 5 shows the values of the different statistical index for the analysed and validation period. RESAT is also compared with the HE for the whole period. Few differences are observed between the analysed and validation periods. POD and FBI perform better during the analysed period, but FAR improves during the validation period. It seems to be a logical behaviour since FBI shows an underestimation of the rainy pixels during validation period and an overestimation during the analysis period. The overestimation leads to better POD scores and the underestimation leads to better FAR scores. The difference in the values of FBI between the analysis and validation period may be due to a major percentage of DCC pixels (associated with high probability of rainfall) in the analysis period.

The entire index performs better in the RESAT than in the HE (table 5). As has been said before, the HE was developed to estimate intense convective rain and in this study has been used different kinds of meteorological situations involving convective storms characterised by the presence of deep convective clouds, but also other cloud systems with presence of cumulus, stratus and warm convective clouds. The HE clearly underestimates the rain pixels as the value $FBI = 0.74$ shows; this can be due to the fact that the HE tends to classify mainly DCC as rainy pixels. Table 6 shows the sensitivity of the cloud type in the rain / no rain discrimination for both RESAT and the HE method for DCC, Cold stratiform clouds and cumulus. The table shows how even RESAT performs better than the HE, similar values of FAR (0,42 RESAT and 0,38 HE) and better scores in the POD (0,65 RESAT as opposed to 0,55 HE) are found in the case of DCC. Both techniques don't score very well in the case of cold stratiform clouds, but clearly RESAT has better ones than POD. The underestimation of rainy pixels in the HE

with a value of FBI = 0,11 as opposed to the RESAT value of FBI = 0,78, leads to a better score of the FAR for the HE in this type of clouds. The differences between both techniques are clear in the case of cumulus clouds where RESAT scores a POD (0,83) clearly higher than the HE (0,16). In short, cloud classification as an input in the algorithm gives better results in the rain/no-rain discrimination, especially in the pixels classified as cold stratiform clouds and growing cumulus, but also in the convective ones.

4.2 Rainfall estimation

The statistical variables used to validate REASAT has been computed for different grid sizes: 5x5 pixels (20x20 km), 9x9 pixels (36x36 km), 15x15 pixels (60x60 km) and 25x25 pixels (100x100 km). The spatial mean rainfall rate has been computed with the estimated rainfall rate; 1 hour cumulated rainfall would lead to better results (Vicente et al., 1998), but the the TRMM satellite does not pass frequently enough to obtain the required data. The rain / no-rain statistical parameters (POD, FAR, ERR and FBI) have been also been computed for the different grid sizes leading to the similar results already discussed. Table 7 shows the results for both the analysed and validation period. The parameters used to validate the estimation method score slightly better during the analysed period, but not with a significant difference. The statistical parameters tend to converge at a similar value in both the analysis and validation period when increasing the grid size, except for the BIAS. In both periods RESAT tends to overestimate (Bias > 0) the value of rainfall, with greater values of the BIAS during the validation. This pattern is also observed in each of the studied cases. RESAT seems to perform reasonably well for a 60x60 km grid size, with a correlation factor of 0,54 in the analysis period and 0,53 in the validation period. The RMSE also decreases when the

grid size increases. The BIAS seems to be independent of the grid size. Figure 7 show the scatter plots of the RESAT estimates for four different grid sizes.

4.2.1. Comparison with Hydroestimator method

Table 8 summarises the values of the statistical parameters computed for both methods during the validation period and figure 8 shows the scatter plots of the RESAT and Hydroestimator estimates for four grid sizes. In general RESAT performs better than the HE with clearly greater correlation coefficients and RMSE in all grid sizes. Even though the BIAS is lower in the case of RESAT than in the case of the HE, it seems to converge in the case of the HE. As has been commented in the last section in the case of RESAT, the BIAS doesn't decrease when the grid size decreases. This behaviour can be explained by the fact that pixels within the same threshold interval belonging to the same cloud type have associated a similar value of rainfall (the small differences would be given during the second step of the estimation), thus the calculation of a spatial mean of the rainfall rate doesn't present high variability when decreasing the grid size.

Figure 9 shows an event during the analysed period with the RESAT and the HE estimations, it is a convective system in a growing phase, located near the Brazilian coast. Both the RESAT estimation and the radar image show how the cold core of the system, with a greater value of expansion.

5. Summary and future work

The satellite rainfall rate estimation technique RESAT has been presented. The algorithm mixes cloud patch and pixel-based techniques and it is compared with the hydroestimator technique (Vicente et al., 1998) that obtains satisfactory results in despite the fact that it doesn't use moisture correction. The Precipitation Radar product of the TRMM satellite is used in the analysis and validation periods in order to design and validate the algorithm respectively. The algorithm discriminates first the raining pixels associating rainfall only with the pixels classified as cumulus, convective clouds or cold stratiform clouds. In order to estimate the rain in those pixels classified as rainy pixels the algorithm uses some radiative and evolution properties of mesoscale convective systems in different brightness temperature thresholds. The MCS is divided in some brightness temperature partitions (using the T_b thresholds) in order to detect the convective cells embedded in the MCS. The properties computed (such as the expansions of the MCS or their mean temperature difference) presents a linear correlation with the mean rainfall rate computed using the TRMM radar data for each MCS in each brightness temperature partition. This permits us to associate an estimated value of rainfall rate to each MCS in each T_b partition. The use of IR-VIS cloud classification gives an important accuracy in both rain/no rain discrimination and rainfall rate estimation. The TRMM radar rainfall rate/brightness temperature relationship and the cumulative TRMM data histograms have a strong dependency on the cloud type. A different parameterisation is set in the algorithm depending on the cloud type. As a result, the rainfall estimation present good results in high temperature ranges.

POD and FBI present better scores during the analysed period (0,61 and 1,06, respectively) than during the validation period (0,55 and 0,81), while FAR scores the worst (0,43 in the analysed period and 0,32 in the validation period) during the analysed period. This behaviour is logical since RESAT overestimates rainy pixels during the analysed period and underestimates during the validation period. The validation has been made for different grid size boxes. All the statistical variables seem to converge at a similar value for the two periods considered when increasing the grid size box, except for the bias, which always is positive, indicating overestimation. The statistical variable shows that RESAT gives satisfactory results from a grid size of 60x60 km, with a correlation coefficient of 0,53 and almost perfect scores of POD (0,94) and FAR (0,07). When compared with the hydroestimator, RESAT always performs better. The use of the cloud classification acquires special importance in the rain/no rain discrimination. Few differences are observed in both methods for cold pixels belonging to convective clouds. These differences increase significantly in RESAT's favour when the methods are compared for cumulus and stratiform clouds with warmer temperatures. RESAT also presents better correlation and lower values of RMSE than the Hydroestimator for all grid size boxes (table 8).

Although RESAT is ready to be operational, some improvements need to be made. The method is only valid for the daytime period; this limitation can be solved by adding a new algorithm using a nocturne cloud classification carried out using the infrared band channels of the GOES satellite. A humidity correction using the outputs of the ETA model will help to produce more accurate rainfall rate estimation.

6. References

- Adler, R. F., and A. J. Negri, 1988: A satellite infrared technique to estimate tropical convective and stratiform rainfall. *J. Appl. Meteor.*, **27**, 30–51.
- Angelis, C. F., W. F. Lima, L. A. T. Machado, and C. A. Morales, 2005: Precipitation observational capabilities at the Brazilian institute for space research. *Anais II International Precipitation Working Group*, Monterey, California, 25–28, Preceedings, 159–168.
- Arkin, P. A., and B. N. Meisner, 1987: The relationship between largescale convective rainfall and cold cloud over the Western Hemisphere during 1982–84. *Mon. Wea. Rev.*, **115**, 51–74.
- Ba, M. B., and A. Gruber, 2001: GOES multispectral rainfall algorithm (GMSRA). *J. Appl. Meteorol.*, **40**, 1500–1514.
- Carvalho, L. M. V. and C. Jones, 2001: A satellite method to identify structural properties of Mesoscale Convective Systems based on Maximum Spatial Correlation Tracking Technique (MASCOTTE). *J. Appl. Meteor.*, **40**, 1683–1701.
- Delgado, G., A. Redaño, J. Lorente, R. Nieto, L. Gimeno, P. Ribera, D. Barriopedro, R. García-Herrera, A. Serrano, 2006: Cloud Cover Analysis Associated to Cut-off Low Pressure Systems using Meteosat Imagery. *Meteor. Atmos. Physics* (in print).
- Ebert, E., M. J. Manton, P. A. Arkin, R. J. Allam, G. E. Holpin, and A. Gruber, 1996: Results from the GPCP algorithm intercomparison programme. *Bull. Amer. Meteor. Soc.*, **77**, 2875–2887.
- Feidas, H., and C. Cartalis, 2001: Monitoring mesoscale convective cloud systems associated with heavy storms with the use of Meteosat imagery. *J. Appl. Meteorol.*, **40**, 491–512.
- Hong, Y., K. Hsu, S. Sorooshian, and X. Gao, 2004: Precipitation Estimation from Remotely Sensed Imagery using an Artificial Neural Network Cloud Classification System. *J. Appl. Meteor.*, **43**, 1834–1852.
- Kidd, C., D. R. Kniveton, M. C. Todd, and T. J. Bellerby, 2003: Satellite Rainfall Estimation Using Combined Passive Microwaves and Infrared Algorithms. *J. Hydrometeorol.*, **4**, 1088–1104.
- Kuligowski, R. J., 2002: A Self Calibrated Real-Time GOES Rainfall Algorithm for Short-Term Rainfall Estimates. *J. Hydrometeorol.*, **3**, 112–130.
- Laing, A. G., J. M. Fritsch, and A. J. Negri, (1999). Contribution of mesoscale convective complexes to rainfall in Sahelian Africa: estimates from geostationary infrared and passive microwave data. *J. Appl. Meteor.*, **38**: 957–964.
- Machado L. A. T., and W. B. Rossow, 1993: Structural characteristics and radiative properties of tropical cloud clusters. *Mon. Wea. Rev.*, **121**, 3234–3260.

_____, W. B. Rossow, R. L. Guedes, and A. W. Walker, 1998: Life cycle variations of mesoscale convective systems over the Americas. *Mon. Wea. Rev.*, **126**, 1630–1654.

_____, and H. Laurent, 2004: The Convective System Area Expansion over Amazonia and its Relationships with Convective System Life Duration and High-Level Wind Divergence. *Mon. Wea. Rev.*, **132**, 714-725.

Mapes B. E., R. A. Houze Jr, 1992: An Integrated View of 1987 Australian Monsoon and its Mesoscale Convective Systems. Part I: Horizontal structure, *Quart. J. Roy. Meteor. Soc.*, **118**, 927-963.

Mathon V., and H. Laurent, 2001: Life cycle of the Sahelian mesoscale convective cloud systems. *Quart. J. Roy. Meteor. Soc.*, **127**, 377-406.

Porcú, F., and V. Levizzani, 1992: Cloud classification using METEOSAT VIS-IR imagery. *Int. J. Remote Sens.*, **13**, 893-909.

Rossow, W. B., and L. C. Garder, 1993: Cloud detection using satellite measurements of infrared and visible radiances for ISCCP. *J. Climate*, **6**, 12, 2341-2369.

Scofield R. A., 1987: The NESDIS operational convective precipitation estimation technique. *Mon. Wea. Rev.*, **115**, 1773–1792.

Schumacher, R. S., and R. H. Johnson, 2005: Organization and Environmental Properties of Extreme-Rain-Producing Mesoscale Convective Systems. *Mon. Wea. Rev.*, **123**, 961-976.

Uddstrom, M. J., and W. R. Gray, 1996: Satellite cloud classification and rain-rate estimation using multispectral radiances and measures of spatial texture. *J. Appl. Meteor.*, **35**, 839–858.

Vicente, G., R. A. Scofield, and W. P. Mensel, 1998: The operational GOES infrared rainfall estimation technique. *Bull. Amer. Meteor. Soc.*, **79**, 1881–1898.

_____, J. C. Davenport, and R. A. Scofield, 2002: The role of orographic and parallax corrections on real time high resolution rainfall rate distribution. *Int. J. Remote Sensing*, **23**, 2, 221-230.

Vila, D. A., L. A. T. Machado, H. Laurent, and I. Velasco, 2005: Forecast and tracking the evolution of clouds clusters (ForTraCC) using satellite infrared imagery: Methodology and validation. Submitted to Journal of Applied Meteorology and Climatology.

Wylie, D. P. 1979: An application of a geostationary satellite estimation technique to an extratropical area. *J. Appl. Meteorol.*, **18**, 1640-1648.

Xu, L., S. Sorooshian, X. Gao, and H. Gupta, 1999: A cloud-patch technique for identification and removal of no-rain clouds from satellite infrared imagery. *J. Appl. Meteor.*, **38**, 1170–1181.

Figure Captions

Table 1: Cases studied during the analysed and validation period.

Table 2: Coefficients values and correlation coefficients of the multiple linear regression to obtain the cluster rainfall estimation for all the Tb thresholds.

Table 3: Coefficients of the third degree polynomial function fitted to obtain the pixel rainfall estimation for all the cloud types.

Table 4: Rate parameters of the frequency distributions of the pixel rainfall estimation values and the radar data for all cloud types.

Table 5: Statistical index describing the accuracy of the rain no rain discrimination of the RESAT method (analysis and validation period) and the hidroestimator method (validation period).

Table 6: Statistical index showing the accuracy of the rain no rain discrimination for different cloud types (deep convective, cumulus and cold estratiform) for both RESAT and hidroestimator methods. Results show how RESAT much performs better in the case of cold estratiform and cumulus cloud types.

Table 7: Statistical index showing the accuracy of the RESAT rainfall estimation fro different grid sizes during the analysis and validation period.

Table 8: Statistical index comparing the rainfall rate estimation of RESAT an hidroestimator for different grid sizes.

Figure 1: Domain chosen for the study. In black the TRMM swath and in blue the precipitation product detected by the Radar for a case of study (November 17 of 2004 at 1415 UTC).

Figure 2: Flow chart of the multilayer tracking algorithm.

Figure 3: Scatterplots between the parameters describing the evolution of the MCS's and its mean rain for a Tb threshold of 230 K. A linear correlation is observed. All the parameters present a negative slope except for the expansion showing a relation between the growth of the MCS's and its potential to produce heavy rainfalls.

Figure 4: Scatterplots between the cluster rainfall rain estimation and the mean rainfall value for every MCS's for all Tb threshold.

Figure 5: Mean value of r_c computed for each 1 K interval of Tv for the six cloud types considered. The curve is fitted with a 3rd degree polynomial function. A different curve is obtained for every cloud type, allowing discrimination between cloud types in the final rainfall estimation.

Figure 6: Frequency distribution of rainfall from radar and the pixel rainfall estimation (Rp) for Deep Convective Cloud pixels. Both distributions will be approximated to an

exponential distribution. The algorithm will fit the R_p distribution into the radar distribution to obtain the final rainfall estimation.

Figure 7: Scatterplot of the RESAT estimates for the analyzed period (left) and validation period (right) for four different grid sizes.

Figure 8: Scatterplot of RESAT (left) and Hidroestimator (right) for 60 X 60 km and 100 X100 km grid size.

Figure 9: Rainfall rate on November 17 of 2004 (1045 UTC). Upper left panel: RESAT; upper right panel: Hidroestimator; lower left panel: Radar.

Table 1

Analysis period		Validation period	
<i>Date</i>	<i>Hour (UTC)</i>	<i>Date</i>	<i>Hour (UTC)</i>
04-11-2004	1945	27-11-2004	1115
05-11-2004	1045	03-12-2004	2045
07-11-2004	1015	08-12-2004	1745
07-11-2004	1645	11-12-2004	1645
07-11-2004	2015	12-12-2004	1715
08-11-2004	2045	17-12-2004	1415
09-11-2004	1645	20-12-2004	1945
09-11-2004	1945	21-12-2004	1345
10-11-2004	1045	22-12-2004	1115
10-11-2004	2045		
12-11-2004	1045		
12-11-2004	1345		
14-11-2004	1015		
17-11-2004	1045		
17-11-2004	1415		
18-11-2004	1445		
20-11-2004	1115		
23-11-2004	1015		

Table 2

<i>250 K</i>	a	b	c	d	e	f
Coef. Value	0.00081	-0.04826	-0.08393	-0.02199	-0.02015	19.24
Correlation	0.32	-0.45	-0.41	-0.46	-0.37	
<i>240 K</i>						
Coef. Value	0.00236	-0.01961	-0.06305	-0.05048	0.00724	18.46
Correlation	0.35	-0.44	-0.28	-0.44	-0.24	
<i>230 K</i>						
Coef. Value	0.00194	-0.07076	-0.17429	-0.01176	-0.01325	21.79
Correlation	0.41	-0.44	-0.46	-0.43	-0.40	
<i>220 K</i>						
Coef. Value	0.00254	-0.11085	-0.12312	-0.10822	-0.02018	2.49
Correlation	0.39	-0.32	-0.35	-0.37	-0.39	
<i>210 K</i>						
Coef. Value	0.00137	0.00720	-0.11989	-0.12744	-0.07376	28.41
Correlation	0.45	-0.41	-0.41	-0.47	-0.48	

Table 3

<i>Cloud type</i>	<i>3rd degree</i>	<i>2nd degree</i>	<i>1st degree</i>	<i>Constant term</i>
Cumulus	3,09*10 ⁻⁴	-64,21*10 ⁻⁴	-0,049499	-0,584657
Convective 3	-2,47*10 ⁻⁴	78,36*10 ⁻⁴	-0,118129	-1,784454
Convective 2	-2,30*10 ⁻⁴	0,014565	-0,215432	-1,047433
Convective 1	4,68*10 ⁻⁴	-0,019028	0,103186	-3,014308
Stratiform	-1,77*10 ⁻⁴	-11,12*10 ⁻⁴	-0,015940	-1,693500
Deep convective	-23,40*10 ⁻⁴	0,037950	-0,074900	-2,930100

Table 4

<i>Cloud type</i>	λ_{Rp}	λ_r
Cumulus	0,98	0,19
Convective 3	1,12	0,18
Convective 2	0,77	0,14
Convective 1	2,13	0,22
Stratiform	2,63	0,24
Deep convective	0,90	0,17

Table 5

	<i>Analysed period</i>	<i>Validation period</i>	<i>Validation HE</i>
POD	0.61	0,55	0,43
FAR	0.43	0,32	0,42
ERR	0,26	0,27	0,33
FBI	1,06	0,81	0,74

Table 6

	<i>DCC</i>		<i>Cold Estrat</i>		<i>Cumulus</i>	
	Method	HE	Method	HE	Method	HE
POD	0,65	0,55	0,45	0,12	0,83	0,16
FAR	0,42	0,38	0,42	0,47	0,39	0,35
ERR	0,43	0,41	0,36	0,45	0,35	0,39
FBI	1,12	0,91	0,78	0,11	1,36	0,25

Table 7

Period	Analysing				Validation			
Grid size (km)	20X20	36x36	60x60	100x100	20x20	36x36	60x60	100x100
Sample size	4460	1781	704	244	1488	524	205	75
Correlation	0,32	0,45	0,54	0,64	0,26	0,39	0,53	0,64
Sat. std dev	2,61	2,26	1,87	1,37	3,42	3,01	2,44	1,90
Radar std dev	2,35	1,86	1,38	0,92	2,76	2,22	1,68	1,24
Rmse	4,45	4,15	3,95	3,99	5,92	5,63	5,23	5
Bias	1,1	1,01	1	1,11	1,63	1,55	1,38	1,42
POD	0,81	0,88	0,94	0,98	0,73	0,81	0,87	0,93
FAR	0,16	0,11	0,07	0,03	0,17	0,13	0,08	0,04
ERR	0,23	0,17	0,11	0,03	0,25	0,2	0,13	0,07
FBI	0,97	1	1,02	1,01	0,89	0,94	0,95	0,97

Table 8

Grid size (km)	Method				Hidroestimator			
	20X20	36x36	60x60	100x100	20x20	36x36	60x60	100x100
Sample size	1488	524	205	75	1488	524	205	75
Correlation	0,32	0,45	0,54	0,64	0,22	0,39	0,41	0,49
Sat. std dev	2,61	2,26	1,87	1,37	5,14	3,76	2,67	1,72
Radar std dev	2,35	1,86	1,38	0,92	2,35	1,86	1,38	0,92
Rmse	4,45	4,15	3,95	3,99	6,01	5,66	5,54	5,56
Bias	1,1	1,01	1	1,11	1,66	1,46	1,37	1,36
POD	0,81	0,88	0,94	0,98	0,64	0,73	0,84	0,93
FAR	0,16	0,11	0,07	0,03	0,18	0,13	0,08	0,03
ERR	0,23	0,17	0,11	0,03	0,39	0,33	0,21	0,09
FBI	0,97	1	1,02	1,01	0,81	0,87	0,92	0,97

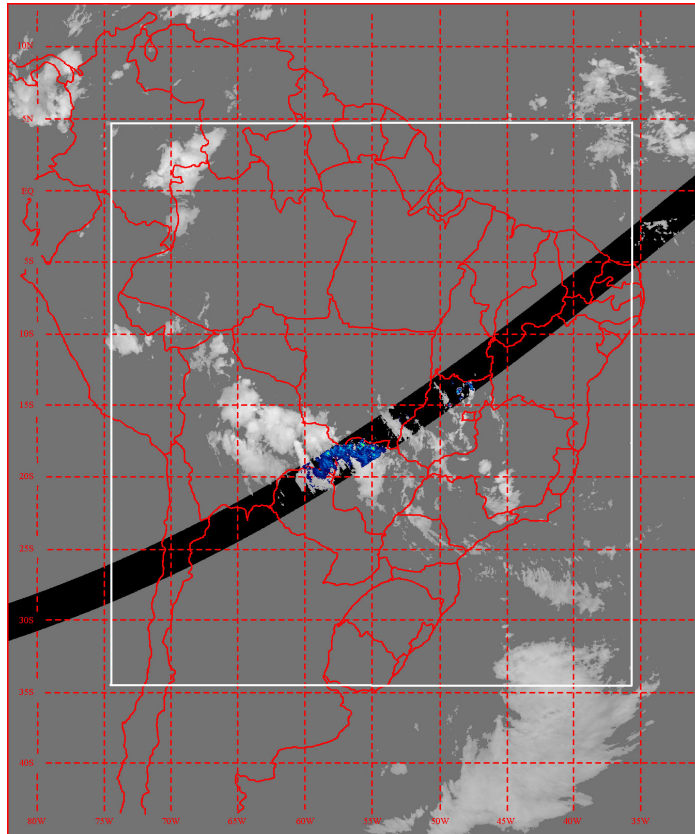


Figure 1

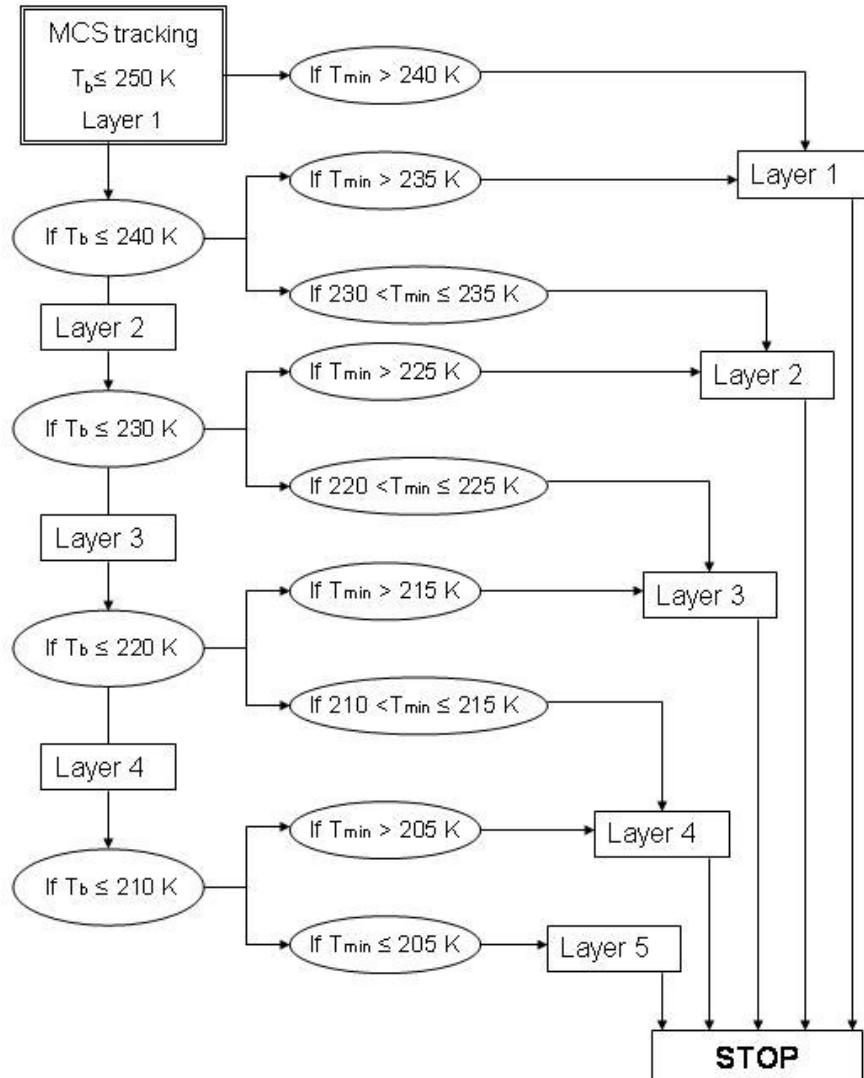


Figure 2

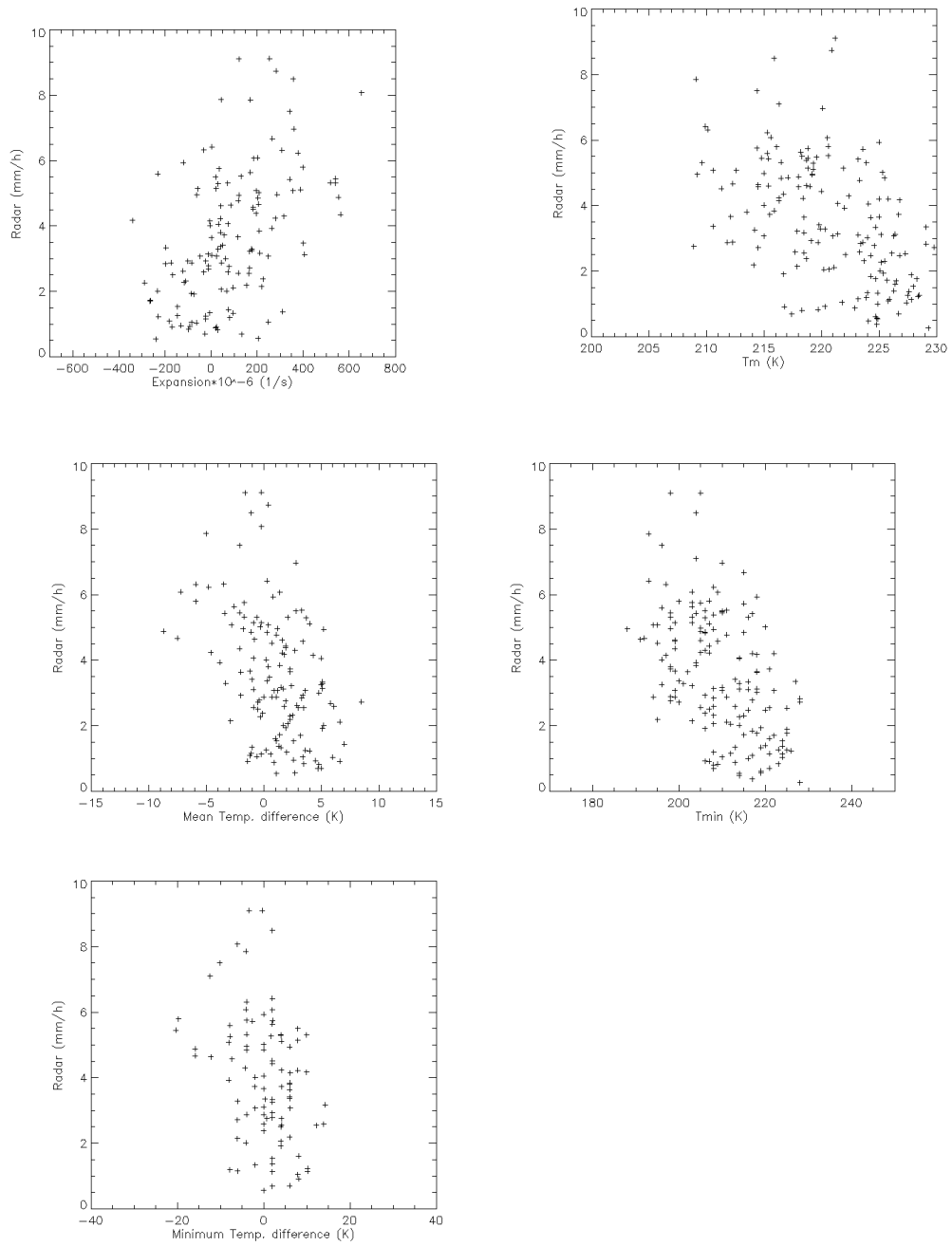


Figure 3

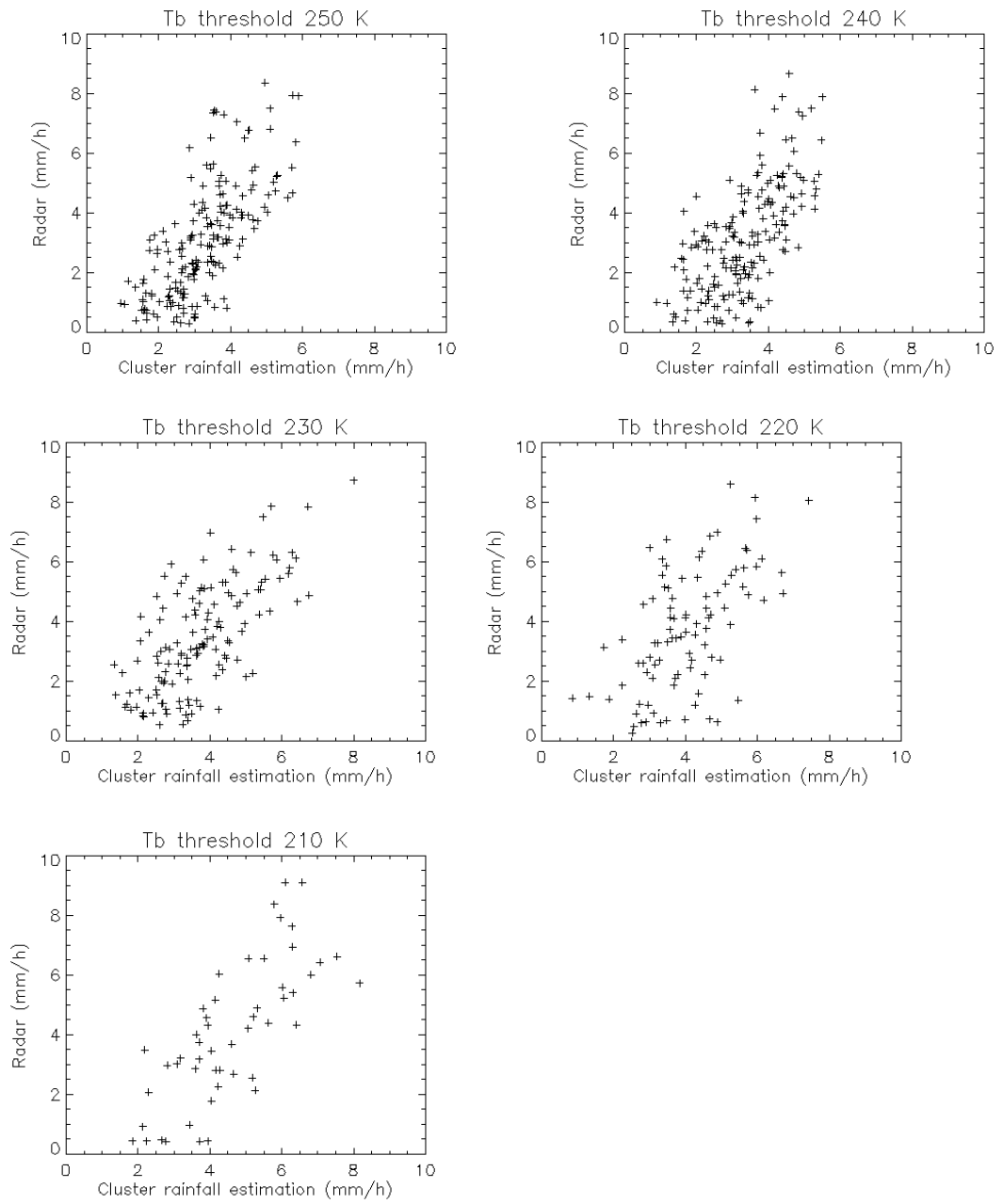


Figure 4

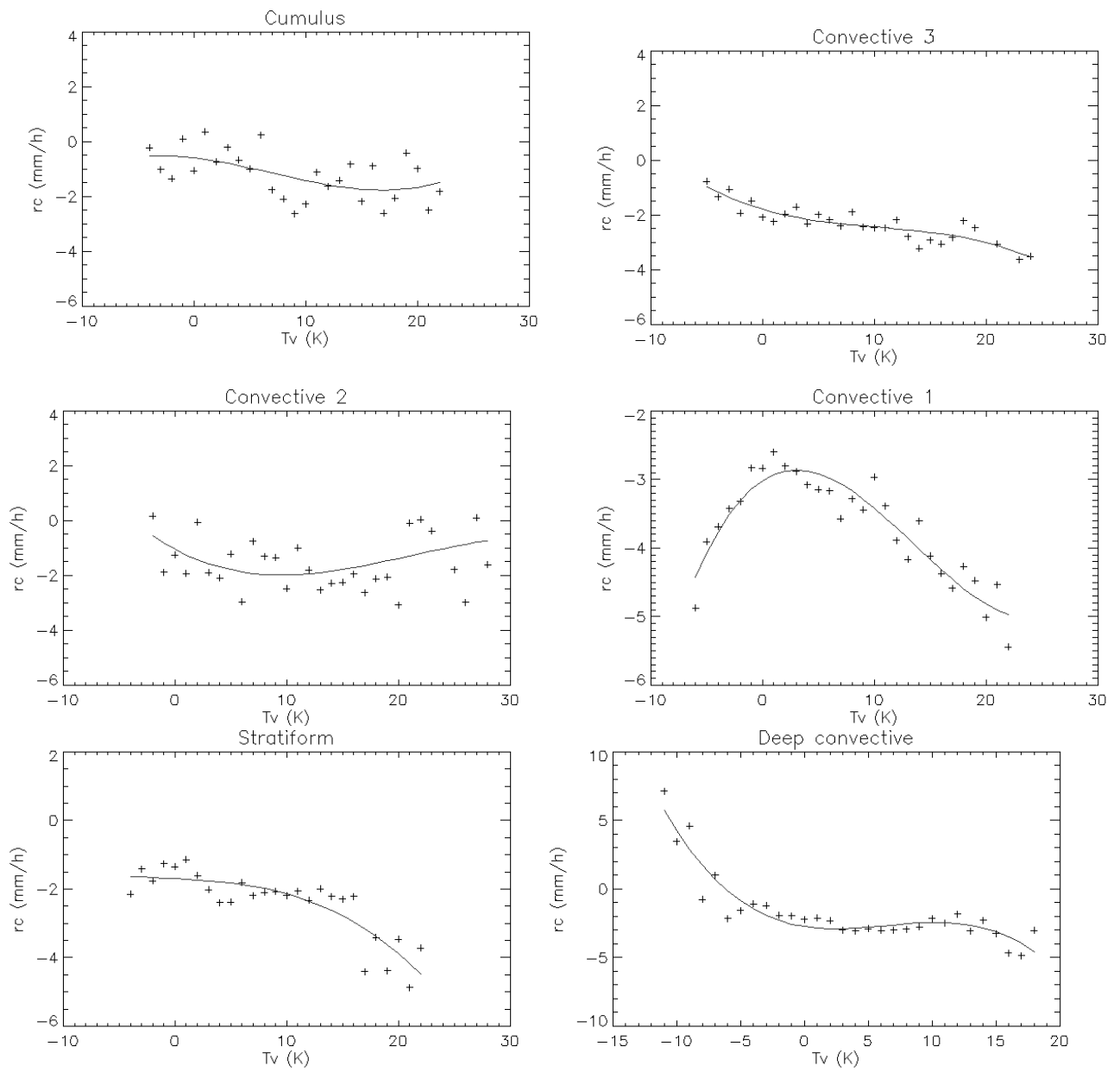


Figure 5

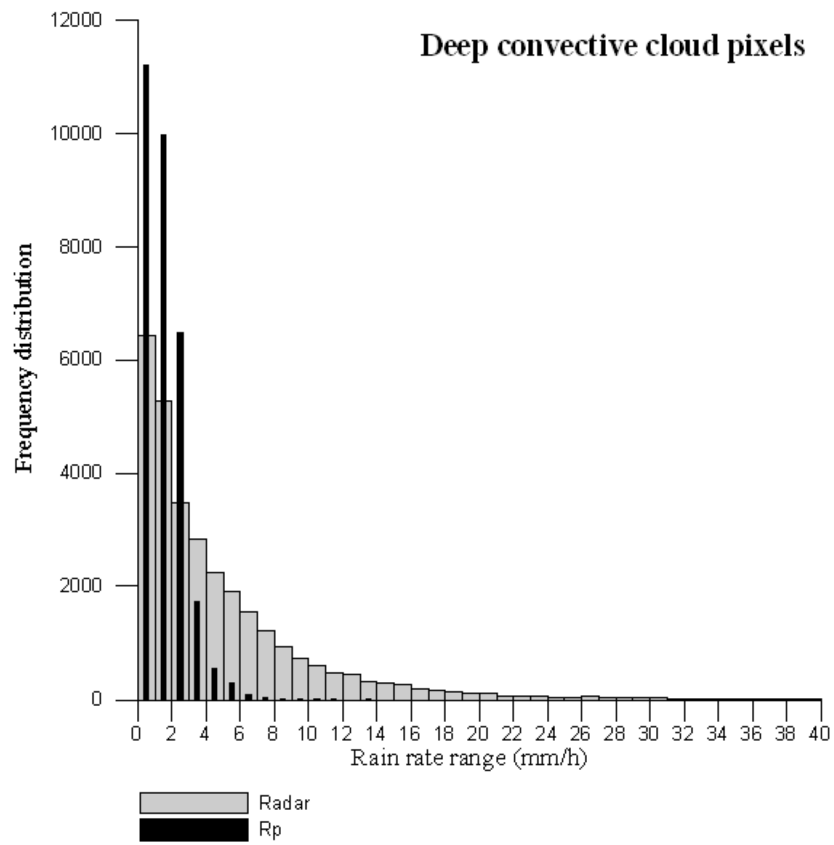


Figure 6

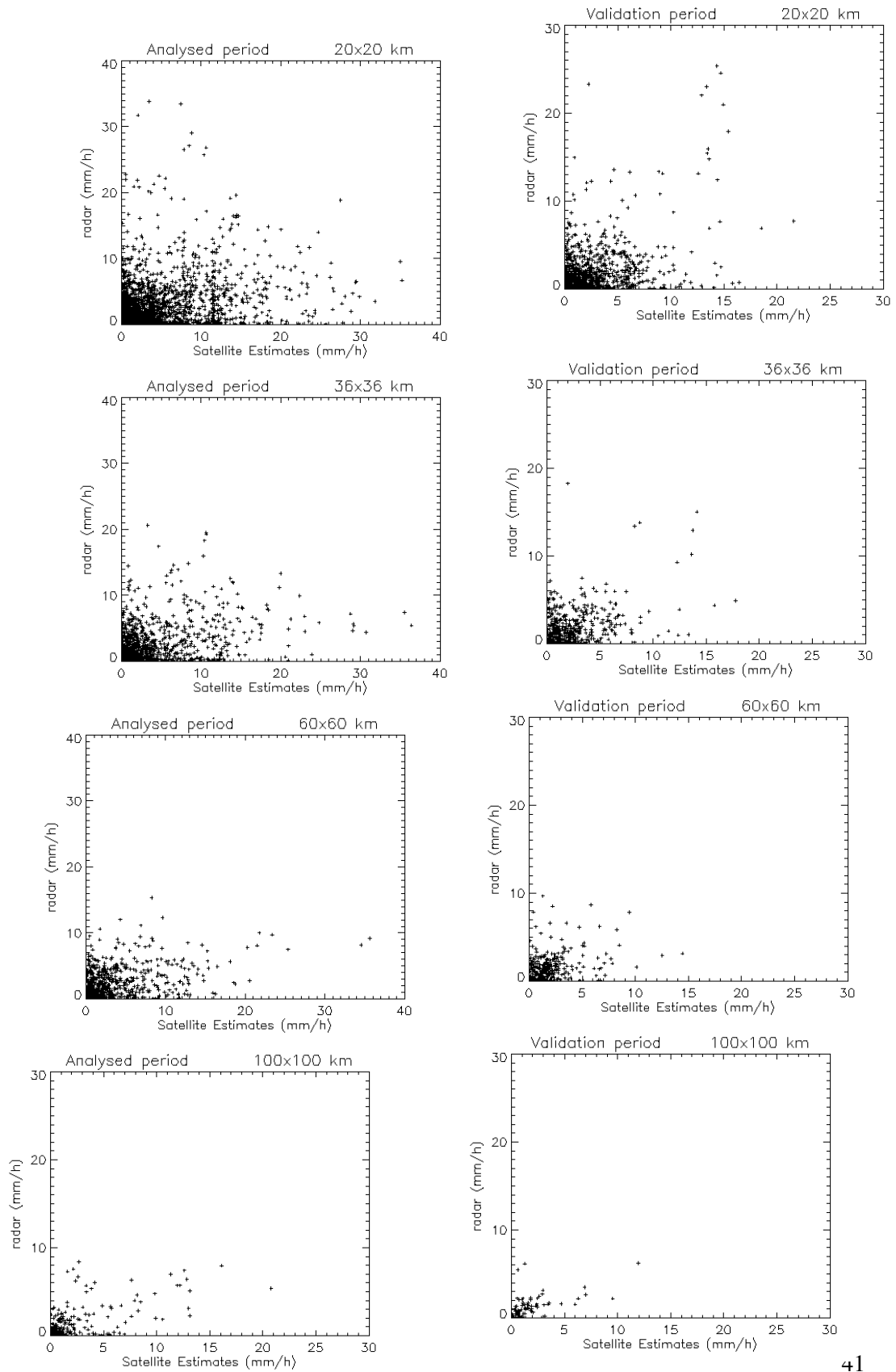


Figure 7

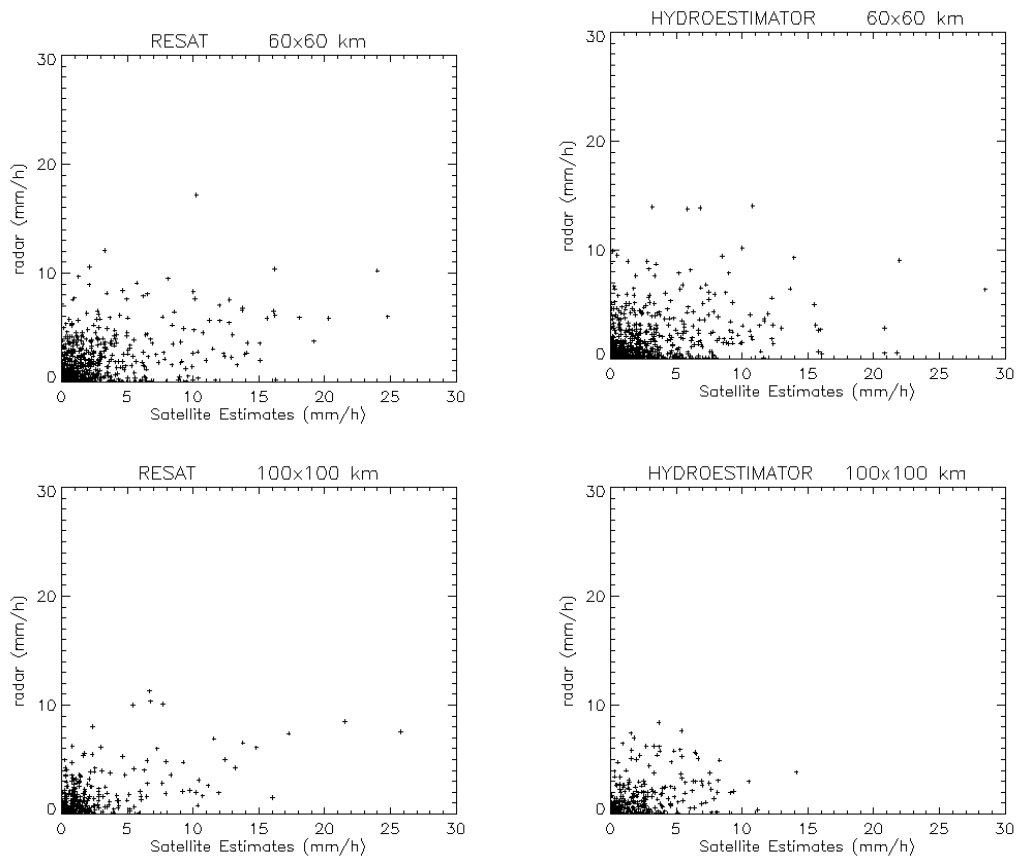


Figure 8

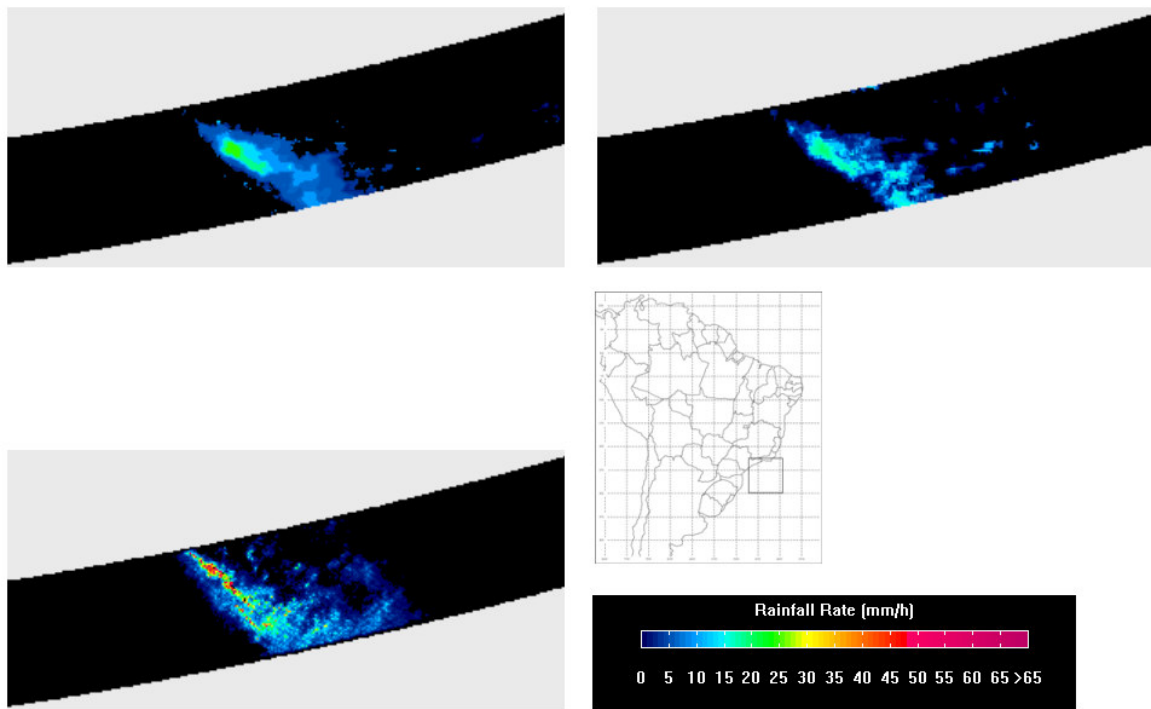


Figure 9

